Science of the Total Environment 682 (2019) 541–552

Contents lists available at ScienceDirect

Science of the Total Environment

journal homepage: www.elsevier.com/locate/scitotenv

Lidar data assimilation method based on CRTM and WRF-Chem models and its application in $PM_{2.5}$ forecasts in Beijing

Xinghong Cheng [a,b], Yuelin Liu [c,d], Xiangde Xu [a], Wei You [e,*], Zengliang Zang [e], Lina Gao [b], Yubao Chen [b], Debin Su [c,d], Peng Yan [b,*]

[a] State Key Lab of Severe Weather, Key Laboratory for Atmospheric Chemistry, Chinese Academy of Meteorological Sciences, Beijing 100081, China
[b] Meteorological Observation Center, Chinese Meteorological Administration, Beijing 100081, China
[c] Key Laboratory of Atmospheric Sounding, Chinese Meteorological Administration, Chengdu 610225, China
[d] College of Electronic Engineering, Chengdu University of Information Technology, Chengdu 610225, China
[e] Institute of Meteorology and Oceanography, National University of Defense Technology, Nanjing 211101, China

HIGHLIGHTS

- The 3DVAR assimilation system of lidar extinction coefficient data developed based on CRTM and WRF-Chem;
- $PM_{2.5}$ forecasts with lidar DA close to observations, while those without DA remarkably underestimated;
- The vertical distribution of $PM_{2.5}$ distinctly improved with lidar DA and significant improvement for nitrate.

GRAPHICAL ABSTRACT

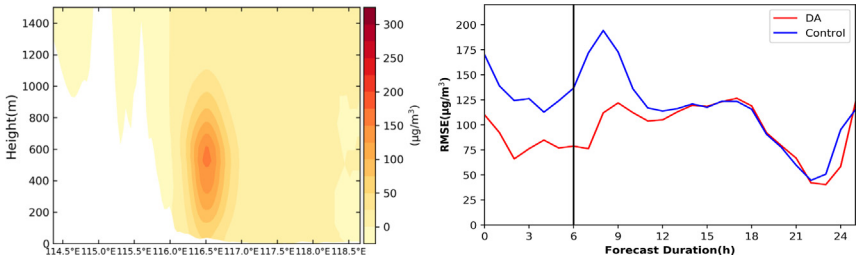

ARTICLE INFO

Article history:
Received 8 April 2019
Received in revised form 11 May 2019
Accepted 13 May 2019
Available online 17 May 2019

Editor: Jianmin Chen

Keywords:
Lidar data assimilation
3DVAR
CRTM
WRF-Chem
$PM_{2.5}$ forecast

ABSTRACT

A three-dimensional variational (3DVAR) lidar data assimilation method is developed based on the Community Radiative Transfer Model (CRTM) and Weather Research and Forecasting model coupled to Chemistry (WRF-Chem) model. A 3DVAR data assimilation (DA) system using lidar extinction coefficient observation data is established, and variables from the Model for Simulating Aerosol Interactions and Chemistry (MOSAIC) mechanism of the WRF-Chem model are employed. Hourly lidar extinction coefficient data from 12:00 to 18:00 UTC on March 13, 2018 at four stations in Beijing are assimilated into the initial field of the WRF-Chem model; subsequently, a 24 h $PM_{2.5}$ concentration forecast is made. Results indicate that assimilating lidar data can effectively improve the subsequent forecast. $PM_{2.5}$ forecasts without using lidar DA are remarkably underestimated, particularly during heavy haze periods; in contrast, forecasts of $PM_{2.5}$ concentrations with lidar DA are closer to observations, the model low bias is evidently reduced, and the vertical distribution of the $PM_{2.5}$ concentration in Beijing is distinctly improved from the surface to 1200 m. Of the five aerosol species, improvements of NO_3^- are the most significant. The correlation coefficient between $PM_{2.5}$ concentration forecasts with lidar DA and observations at 12 stations in Beijing is increased by 0.45, and the corresponding average RMSE is decreased by 25 $\mu g \cdot m^{-3}$, which respectively compared to those without DA.

1. Introduction

Aerosol data assimilation (DA) is a statistically optimal approach that combines observations with numerical model outputs to reduce

* Corresponding authors.
E-mail addresses: ywlx_1987@163.com (W. You), yanpeng@cma.gov.cn (P. Yan).

https://doi.org/10.1016/j.scitotenv.2019.05.186
0048-9697/

uncertainties in the initial fields of the Chemical Transport Model (CTM) (Liu et al., 2011). Since 2001, many studies have utilized different DA methods to improve simulations of the temporal-spatial distribution of aerosols (Collins et al., 2001), and results have shown that the analyses field with aerosol DA is skillful at fitting the observations and improving subsequent forecasts of aerosol and its species.

Most researchers have assimilated surface $PM_{2.5}$ or PM_{10} in-situ observations using a three-dimensional variational (3DVAR) approach (Denby et al., 2008; Tombette et al., 2009; Pagowski et al., 2010; Pagowski and Grell, 2012; Li et al., 2013), four-dimensional variational (4DVAR) (Morcrette et al., 2009; Mangold et al., 2011) approach, or the ensemble Kalman filter (EnKF) approach (Lin et al., 2008). Other researchers have assimilated satellite-derived aerosol products in global and regional CTMs using similar optimal interpolation (OI) (Yu et al., 2003; Generoso et al., 2007; Adhikary et al., 2008), two-dimensional variational (2DVAR) (Zhang et al., 2008), 3DVAR (Niu et al., 2008; Liu et al., 2011; You, 2017), 4DVAR (Benedetti et al., 2009), or EnKF (Schutgens et al., 2010) techniques. However, one of the limitations of these previous studies is that when using surface or satellite-derived observations, aerosol vertical profile information is not included, which means that it is not possible to improve the 3D structure of aerosols.

Therefore, to improve the 3D structure of aerosol and extend the temporal influence of DA, it is necessary to assimilate vertical profile observations (Wang et al., 2013; Zang et al., 2016). In this respect, to improve the simulation and forecasts of aerosol vertical distributions with CTMs, some scientists have investigated the aerosol DA method using 3D measurements from the following: space-borne active instruments on board of CALIPSO over East Asia and the United States of America (Sekiyama et al., 2010; Zhang et al., 2011); 3D profiles of aircraft speciated observations in the USA (Zang et al., 2016); ground-based lidar observations at several observatories in Japan (Yumimoto et al., 2008; Sugimoto and Uno, 2009); measurements from the European Aerosol Research Lidar Network (EARLINET) (Wang et al., 2013); and direct lidar signals from EARLINET (Wang et al., 2014a, 2014b).

Compared with the relatively large retrieval errors from satellite observations and discontinuous aircraft-speciated observations, ground-based lidar measurements are more accurate. As they are conducted continuously throughout the day and night, lidar DA measurements are more suitable for use in improving the analysis and forecast of the 3D distribution of aerosols by CTMs. In this respect, Yumimoto et al. (2007, 2008) used a 4DVar data assimilation system for Asian dust to assimilate extinction coefficient data from ground-based lidar at several stations in Japan. In addition, Wang et al. (2013) compared the efficiency of assimilating lidar and in situ surface measurements to improve PM_{10} forecasts over Europe, and suggested that assimilation of lidar observations may be more efficient for improving PM_{10} forecasts, although it depended on the number of lidar stations employed. Wang et al. (2013) did not directly assimilate the lidar extinction coefficient or aerosol optical depth (AOD), and used a relation between the mass concentration and optical properties of aerosols. Then they determined that the direct assimilation of lidar signals in CTMS provides more accurate results, as uncertainties in the lidar signal are very small (Wang et al., 2014a). In addition, Wang et al. (2014b) evaluated lidar signals simulated by the POLYPHEMUS model and developed a DA algorithm for assimilating lidar signals using the OI method.

A few researchers have recently begun to investigate the lidar DA method and its application in aerosol simulation and forecasts in China. For example, Xiang (2018) assimilated lidar measurements based on the relation between $PM_{2.5}$ concentrations and the aerosol extinction coefficient from 12 lidar stations and two vehicle mobile lidars in the Beijing-Tianjin-Hebei (BTH) region using the gridpoint statistical interpolation (GSI) assimilation system, which is developed by the National Center for Atmospheric Research (NCAR). Furthermore, Zheng (2018) firstly assimilated ground $PM_{2.5}$ observations at 490 stations into the initial field of the NAQPMS model in the BTH region using the OI method, and then used aerosol extinction coefficient profiles observed by 12 lidar stations and the assimilated $PM_{2.5}$ concentration field in the second layer, with the aim of correcting $PM_{2.5}$ concentrations in other model layers. However, both of these studies have limitations: the relationship between $PM_{2.5}$ concentrations and the aerosol extinction coefficient from lidar is unstable, and the errors in retrieved $PM_{2.5}$ concentrations are large. In addition, vertical information from lidar is not assimilated into the WRF-Chem model (Grell et al., 2005) through a statistics technique (Xiang, 2018). Although Zheng (2018) used vertical profiles of the aerosol extinction coefficient to correct the modelled $PM_{2.5}$ concentration in the upper layers of the NAQPMS model, he hypothesized that the vertical distribution characteristics of $PM_{2.5}$ and the aerosol extinction coefficient were the same. However, optical properties are obviously affected by humidity and the size distribution of aerosol species in $PM_{2.5}$; therefore, such a hypothesis is not applicable for lidar DA to a certain degree.

To directly assimilate the vertical profiles of aerosol extinction coefficients into the CTM model, it is critical to use the radiative transfer model to establish an observation operator between the simulated mass concentrations of aerosol species and the extinction coefficient. The Community Radiative Transfer Model (CRTM) and its tangent-linear, adjoint model (Han et al., 2006; Liu and Weng, 2006) were developed at the United States Joint Center for Satellite Data Assimilation (JCSDA). The CRTM not only provides the forward AOD model with fourteen aerosol species simulated using the GOCART aerosol scheme in WRF-Chem model, but also with calculations of the tangent-linear and adjoint models. The CRTM model can calculate aerosol optical depth (AOD), backscatter and extinction coefficient of several main aerosol species considering different types (scattered and absorbing aerosol) and size bins (four or five bins).

However, the CRTM is focused on the GOCART scheme; therefore, for the MOSAIC scheme, we developed a new lidar assimilation method based on the CRTM model and 3DVAR techniques, and directly assimilated vertical profiles of aerosol extinction coefficients from four lidars into the initial field of WRF-Chem model in Beijing, with the aim of improving the forecast of $PM_{2.5}$ 3D distribution. This paper is organized as follows: Section 2 describes the experimental setup, including the lidar field experiment and model settings; Section 3 presents construction of the background error covariance, the new lidar observation operator, and the DA experiment; Section 4 describes evaluation of the DA analysis and forecast of $PM_{2.5}$ based on surface measurements; and the findings are then summarized and discussed in Section 5.

2. Experimental setup

2.1. Field experiment

To validate the improvement effect of assimilating lidar data, lidars were installed at four principal national weather stations in the northwest, southwest, central, and southern area of Beijing respectively, to observe aerosol optical depth (AOD), backscatter, and extinction coefficient data during a pollution episode from March 13 to 15, 2018. Prior to the experiment, a parallel observation using four lidars was conducted at Nanjiao (NJ) station in Beijing from September to November 2017, to obtain comparable data. Parallel observation results showed that extinction coefficients from four lidars and their temporal variations are consistent, and relative standard deviation of backscatter coefficient from surface to the height about 2000 m were all lower than 20.4%. Fig. 1 shows the model domain of the simulation experiment together with the distribution of the four in-situ lidars and 12 $PM_{2.5}$ monitoring stations of the National Environment Monitoring Station in China (China National Environmental Monitoring Center, CNEMC, 2012). The lidar observation parameters are listed in Table 1. To reduce the error related to the inversion algorithm, all extinction coefficient data were derived from the four lidar signals using the same SCC algorithm

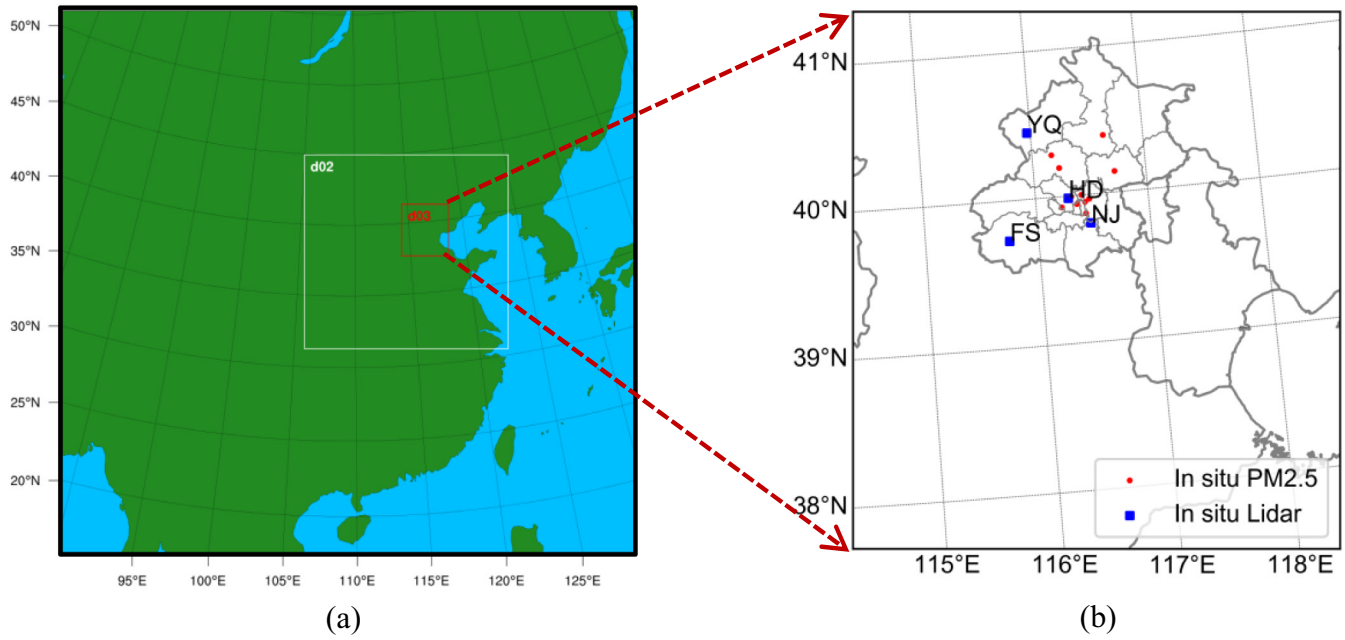

Fig. 1. Triple-nested model domains (a) and distribution of in-situ lidar and 12 $PM_{2.5}$ stations (b) within the inner domain (marked by D03), which covers Beijing, Tianjin and the central part of Hebei province.

(Böckmann et al., 2004) which is usually employed in the EARLINET. Two Raman and two Mie types of Lidar were used, and wavelengths of 532 nm were employed. Hourly vertical profile of extinction coefficient data at the four stations were assimilated in the initial field of the WRF-Chem model, and the vertical resolution was normalized to a height of 15 m. The vertical layers from 150 to 2000 m were selected for assimilation in consideration of the impact of the blind zone and cloud.

2.2. Validation of lidar data

To validate the reliability of lidar data, we analysis the temporal variation characteristics of the lidar (Fig. 2) compared to surface $PM_{2.5}$ concentration (Fig. 3a, b) and visibility (Fig. 3c) observed at the NJ and HD station on Mar. 12–15, 2018. Extinction coefficients between 150 m and 2000 m during 15:30–19:30 UTC on March 13 at NJ station and those between 150 m and 1500 m during 21:00 UTC on March 13–4:00 UTC on March 14 at HD station were found to be higher than those at other times. In particular, those between 400 m and 1500 m at 16:00 UTC on March 13 at NJ station and 2:00 UTC on March 14 at HD station were the highest at ~3.5 km^{-1}. The corresponding $PM_{2.5}$ concentrations for the same period at two stations were also higher, but visibilities at NJ station were lower. The $PM_{2.5}$ concentration corresponding to the largest extinction coefficient reached the highest values, with respectively 400 and 300 $\mu g \cdot m^{-3}$ at NJ and HD stations, whereas visibility at this time was the lowest at 1303 m. The results showed that lidar data are able to represent temporal variations of air quality, especially that of heavy haze; therefore, following quality control tests, it was considered effective for use in data assimilation. It is worth noting that in order to reduce the impact of blind area, we assimilate extinction coefficients data above the height of 150 m to the initial field of WRF-Chem model, and extinction coefficients from surface to the height of 150 m is same as those at the height of 150 m in the lidar DA experiment referring the treatments of other researches.

Table 1
Lidar parameters at four stations.

	Nanjiao (NJ)	Haidian (HD)	Yanqing (YQ)	Fangshan (FY)
Type	Raman	Raman	Mie	Mie
Wavelength (nm)	532	532	532	532
Sample frequency (min)	5	10	5	5
Vertical resolution (m)	7.5	15	7.5	3.75
Blind height (m)	100	150	75	75

2.3. Model setup

In this study, the WRF-Chem model was used to simulate concentrations of multiple aerosol species and their spatiotemporal variations over Beijing and its surrounding area on March 12–15, 2018. The Carbon Bond mechanism, version Z (CBMZ), gas-phase chemistry mechanism, and the MOSAIC scheme for aerosol simulation were also selected (Fast et al., 2006). The size distribution was divided into four discrete size bins defined by their lower and upper dry particle diameters. Aerosol species in the MOSAIC (4 bin) scheme include elemental/black carbon (EC/BC), organic carbon (OC), nitrate (NO_3^-), sulfate (SO_4^{2-}), chloride (Cl^-), ammonium (NH_4^+), and sodium (Na^+). Other unspecified inorganic species such as silica (SiO_2), other inert minerals, and trace metals were lumped together as "other inorganic mass" (OIN) (Li et al., 2013; Grell and Freitas, 2014). This study focuses on Beijing at a spatial resolution of 3 km × 3 km with 41 vertical layers of varying thickness (between the surface and 10 hPa) using the triple-nested simulation technique with a horizontal resolution of 27 km, 9 km, 3 km (Fig. 1), and a temporal output interval of 1 h. The WRF-Chem simulations were driven by the FNL/NCEP analysis data every 6 h with a spatial resolution of 1° × 1°. The MEIC aerosols and trace gases emission inventory for 2012 with a resolution of 0.25° × 0.25° were employed (Zhang et al., 2009; Zhao et al., 2015). Initial and boundary conditions for the chemical species in the WRF-Chem were extracted from the output of the MOZART-4 global chemical transport model (Emmons et al., 2010). The simulation was conducted from 00:00 UTC on March 13 to 00:00 UTC on March 15, 2018, with a 12-h spin-up time. Outputs from

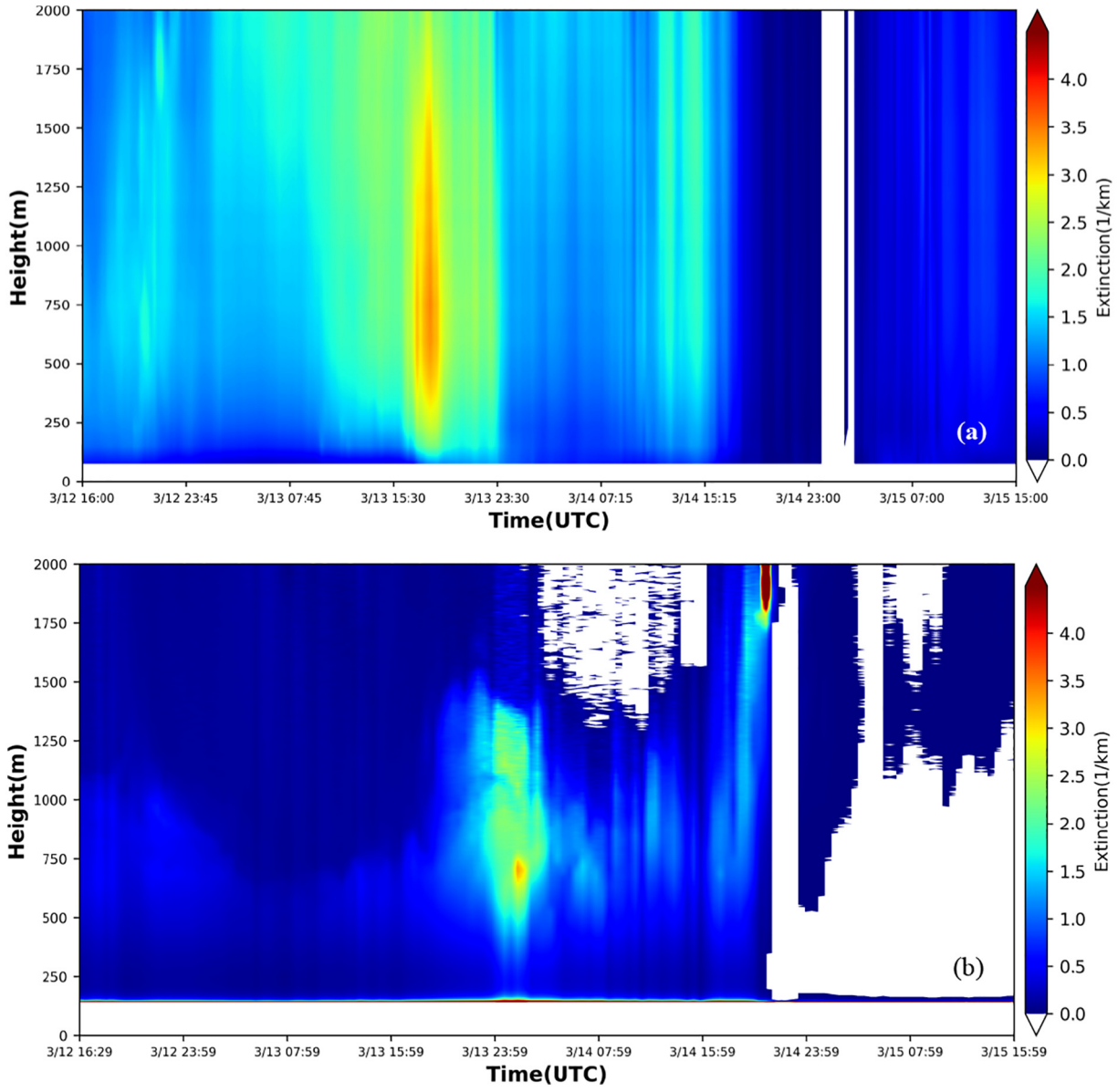

Fig. 2. Time serial of vertical profile of aerosol extinction coefficient from lidar at NJ (a) and HD (b) station on March 12–15, 2018.

the WRF-Chem model on 12:00 UTC on March 13 were used as the initial and boundary conditions for the entire run.

The following parameterization schemes of physical processes within the WRF-Chem model were used in this study: the WRF single-moment 6-class microphysics scheme (WSM6, Hong and Lim, 2006), the RRTMG longwave and shortwave radiation scheme (Iacono et al., 2008), the revised Monin–Obukhov surface layer scheme (Jiménez et al., 2012), the Grell-Freitas convective parameterization scheme (Grell and Freitas, 2014), the Noah land-surface scheme (Chen and Dudhia, 2001), and the Yonsei University (YSU) atmospheric boundary layer scheme (Hong and Lim, 2006).

3. Methodology

3.1. Primary formulation of 3DVAR method

The cost function of 3DVAR can be defined by the objective function being proportional to the square of the distance between the control variable vector, the background state variable vector, and the observation innovation vector (Lorenc, 1981; Parrish and Derber, 1992), and it can be written as:

$$J(x) = \frac{1}{2}(x + x_b)^T B^{-1}\left(x - x^b\right) + \frac{1}{2}(Hx - y)^T R^{-1}(Hx - y) \quad (1)$$

where x is the control variable with the N-vector, and it denotes concentrations of the eight aerosol species in this paper; x^b is the forecast or background state of the eight species generated by the MOSAIC scheme; and B is the N × N-matrix, which denotes the background error covariance (BEC) associated with x. In addition, the M-vector, y, is an observation vector that is the extinction coefficient for every vertical layer observed by the lidars in this work, and the M × M-matrix, R, is the observation error covariance. Furthermore, H is the observation operator that computes the observation estimates from the state variables. The incremental form is generally used to resolve the minimizing cost function of 3DVAR. To simplify computing, the BEC for eight aerosol species

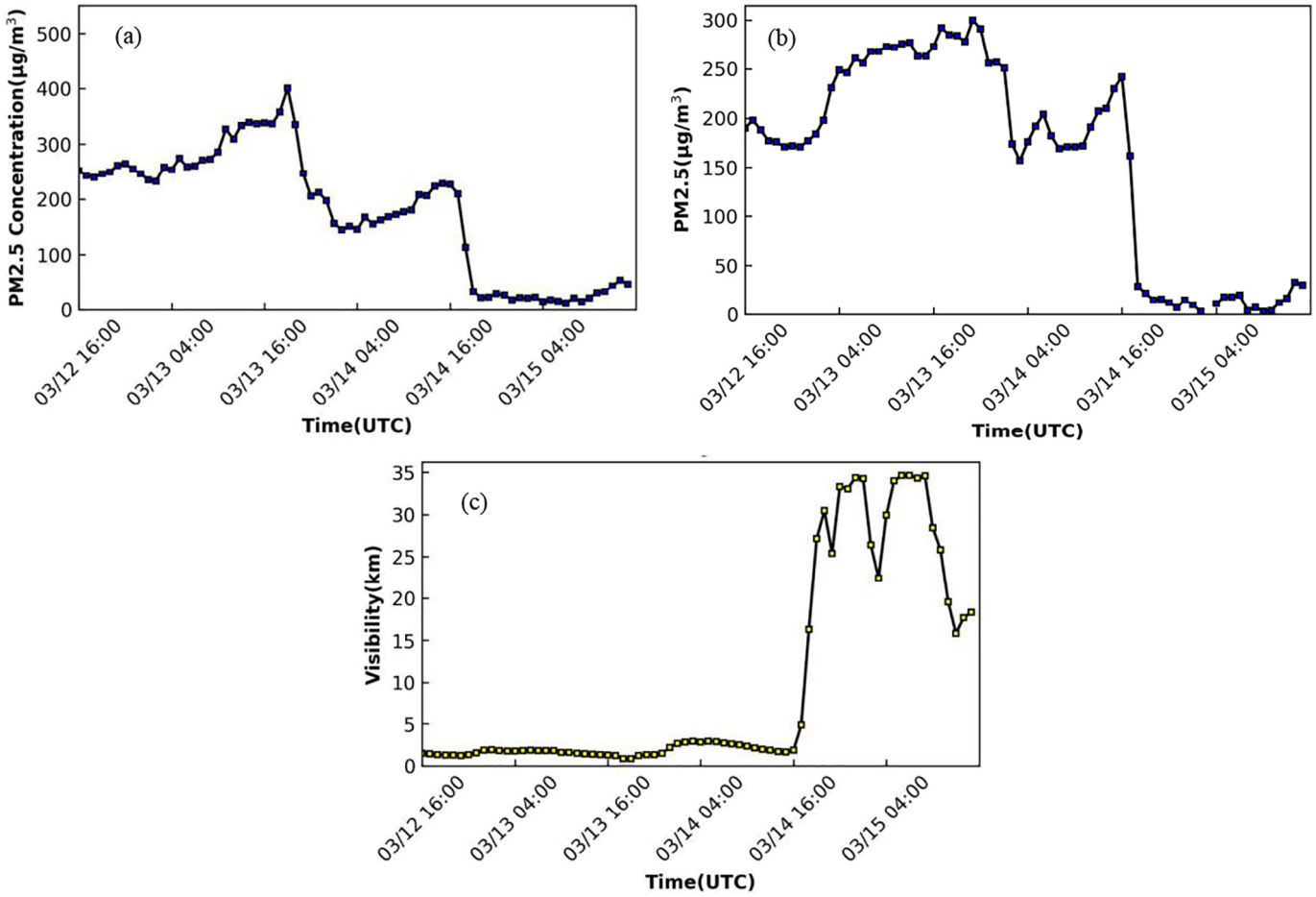

Fig. 3. Time serial of observed $PM_{2.5}$ at NJ (a) and HD (b) station, and visibility at NJ (c) station on March 12–15, 2018.

simulated by the WRF-Chem model can be factorized into two parts following the process outlined by Li et al. (2013) and Zang et al. (2016) as

$$B = DCD^T \quad (2)$$

where D is the standard deviation matrix and C is the correlation matrix. With this factorization, D and C can be prescribed and calculated separately. D is a diagonal matrix whose elements are the standard deviation (SD) of all state variables in the 3D grids, and three-dimensional D is used to improve the capability of the 3DVAR in representing aerosols on small-scales, which vary vertically and are heterogeneous in the horizontal. The static BEC (B) is computed via the "National Meteorological Center (NMC)" method (Parrish and Derber, 1992), by taking the differences between the 48 h and 24 h WRF-Chem forecasts that are valid at the same time over March 2018. Additionally, the observation error, R, is estimated using half of D.

Fig. 4 shows the decrease in correlation curves calculated by the forecast differences with horizontal distance. The cross between the correlation curve and the line of exp(−1/2) (black line) represents the horizontal length scale (L_s), and the L_s of six species falls between 30 and 60 km, where those of NH_4^+, NO_3^-, SO_4^{2-} are longer than other species. Of the six species, the L_s of NH_4^+ is the longest, and that of OIN is the shortest, and it is known that uneven distributions of the six species may result in differences in L_s (Zang et al., 2016).

The vertical profiles of the domain averaged standard deviation (SD) under a height of 10 km for the six species are shown in Fig. 5. It is evident that the SDs differ among the species: the largest SD is associated with SO_4^{2-} and the smallest is associated with EC. Vertical distributions of the SD for all species show a relatively rapid decrease with height. Li et al. (2013) also used the NMC method to calculate BEC statistics for the same aerosol species in the U.S. from the WRF-Chem model, and the shape of the root-mean-squared error (RMSE) profile in their statistics (Li et al., 2013, Fig. 2) is consistent with the results of our statistics.

3.2. Observation operator of lidar extinction coefficient

To compute the observation operator between the control variable and the observation vector for every vertical layer, the CRTM and its tangent-linear, adjoint model are used in this paper. The CRTM was

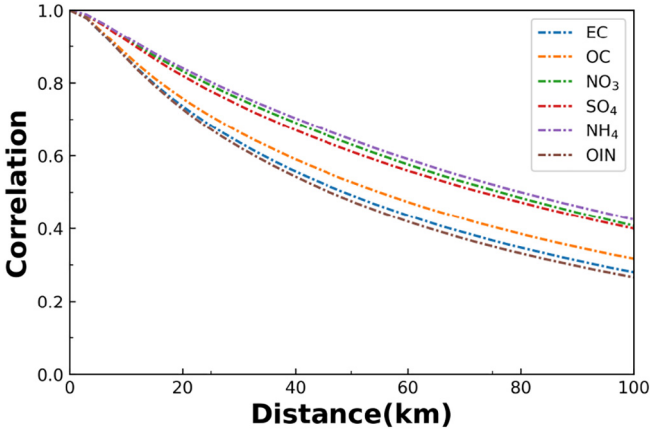

Fig. 4. Horizontal correlation curves of background error for main species in $PM_{2.5}$. Black solid line denotes the length scale at a position of exp(−1/2).

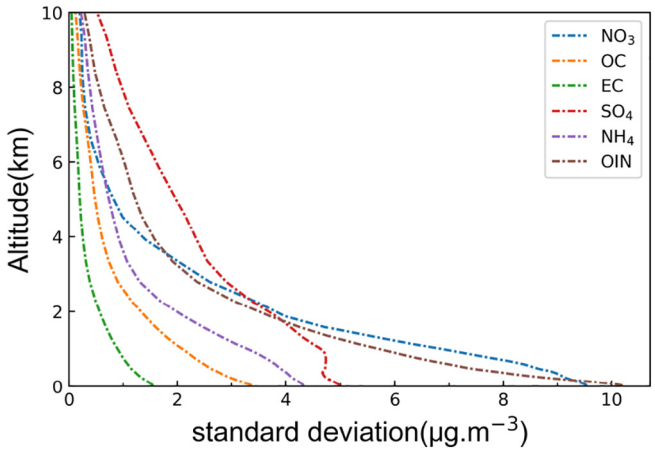

Fig. 5. Profiles of domain-averaged background error standard deviation for main species in $PM_{2.5}$.

Table 2
Aerosol species using the MOSAIC scheme in WRF-Chem and their mapping to the GOCART scheme in CRTM.

Aerosol species in WRF-Chem (sectional)	GOCART aerosols in CRTM (bulk and sectional)
$SO_4^{2-} + NO_3^- + NH_4^+$ (sum of four bins for three species)	SO_4^{2-} (bulk scheme, no size)
OC (sum of four bins)	OC (bulk scheme, no size)
BC (sum of four bins)	BC (bulk scheme, no size)
OIN (sum of four bins)	Dust (sectional scheme, five bins)
$Cl^- + Na^+$ (sum of four bins for two species)	Sea salt (sectional scheme, four bins)

primarily designed for computing satellite radiances; it was used to directly assimilate radiances from multiple infrared and microwave sensors and was then applied to assimilate satellite-derived aerosol products. We extend the CRTM to compute the extinction coefficient using aerosol profiles simulated by the WRF-Chem model, the Jacobian of extinction coefficient with respect to aerosol mass concentrations in every model layer, and vertical profiles of the extinction coefficient observed by lidar (hereinafter referred to as the vertical-layer CRTM-AOD). The forward vertical-layer CRTM-AOD model can derive the extinction coefficient on every model layer with aerosol mass concentration profiles simulated by the GOCART scheme in the WRF-Chem model, and it can simultaneously calculate the gradient of the cost function in 3DVAR analysis, which measures the distance of the state vector to the background and observations. When the cost function is minimized, increments of the extinction coefficient on every model layer can be allocated to 3D profiles of control variables, and the assimilated and updated 3D profiles of control variables (fourteen aerosol species in GOCART scheme) can then be obtained.

To obtain assimilated aerosol profiles for the MOSAIC (4 bin) scheme, it is necessary to transfer the control variables between the GOCART and MOSAIC scheme. Following You (2017), aerosol species in the MOSAIC scheme were mapped to the GOCART scheme of CRTM, as shown in Table 2. It is worth noting that the assimilation treatments of NO_3^- and NH_4^+ are the same as SO_4^{2-} because the optical characteristics of SO_4^{2-} are similar to those of NO_3^- and NH_4^+ (Li et al., 2013; Zang et al., 2016; You, 2017). In this paper, we firstly compute the BECs with the MOSAIC (4 bin) scheme in WRF-Chem and then transfer them to the aerosol species in the GOCART scheme, and we finally assimilate the vertical profiles of the lidar extinction coefficient to the initial field in the WRF-Chem model based on the forward vertical-layer CRTM-AOD model and its Jacobian. Fig. 6 shows a schematic diagram of lidar extinction coefficient assimilation.

3.3. Simulation experiments

To assess the lidar data assimilation analyses and subsequent predictions, results from experiments with and without lidar data assimilation (hereinafter referred to as DA and NoDA experiments, respectively) are

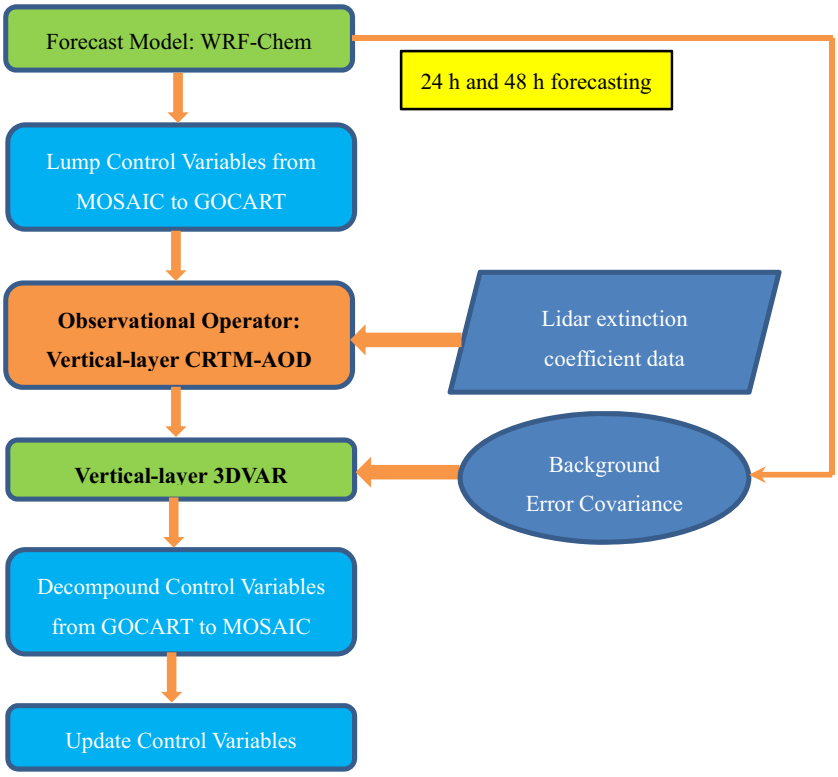

Fig. 6. Schematic diagram of lidar extinction coefficient DA.

compared to observations. The control experiment was conducted from 00:00 UTC on March 13 to 00:00 UTC on March 15, 2018, and the first 12 h of the forecast was discarded as a model spin-up for meteorological and chemical fields. The lidar data assimilation experiment was conducted for 12:00 UTC to 18:00 UTC on March 13, and hourly lidar extinction coefficient profiles at four stations were assimilated. Specifically, the data assimilation was conducted at 12:00 UTC after the above-mentioned spin-up, and the aerosol analysis obtained was then used as the initial condition at 12:00 UTC for the next hour's forecast, which generated the background state for aerosol DA at 13:00 UTC. In this way, the data assimilation and forecast cycle were continuously improved. After continuous DA from 12:00 to 18:00 UTC was finished, the final assimilated analysis field recorded at 18:00 UTC was utilized as the initial condition to forecast the following 30 h (until 00:00 UTC on March 15). In this paper, only extinction coefficient data from four in-situ lidars were assimilated to investigate improvements from lidar DA, and singular values in lidar data caused by cloud and other noise were eliminated before DA. In addition, $PM_{2.5}$ observation data at 12 stations in Beijing were employed to evaluate the assimilated analysis and forecast field. Furthermore, to avoid any differences in the meteorological fields between the control and lidar DA experiment, aerosol feedback to radiation and cloud processes was turned off.

4. Results

4.1. Assessment of data assimilation analysis

Fig. 7 shows the distribution of average $PM_{2.5}$ concentrations from NoDA and DA experiments, associated increments, and surface observations during 12:00–18:00 UTC on March 13, 2018. The spatial distribution characteristics of modelled $PM_{2.5}$ concentrations from the NoDA and DA experiments are consistent with those of observations: they are higher in Beijing than the surrounding areas, and this is related to the higher emissions, unfavorable meteorological conditions, and pollutants transmission from the south during heavy haze period. However, the modelled $PM_{2.5}$ concentrations from the NoDA experiment in Beijing are lower than those from the DA experiment and observations, particularly in northwest and south central Beijing. When lidar DA is applied, the modelled $PM_{2.5}$ concentrations are also closer to observations, and there is positive increment in the area underestimated with NoDA (Fig. 7c). In addition, the simulated $PM_{2.5}$ concentrations with DA are remarkably improved in high layers such as 925 hPa (Fig. 8) compared to NoDA, and there is an obvious positive increment in northwest and south-central Beijing (Fig. 8c).

We also analyzed the spatial distribution characteristics of increments of five main species in $PM_{2.5}$ using lidar DA (as shown in

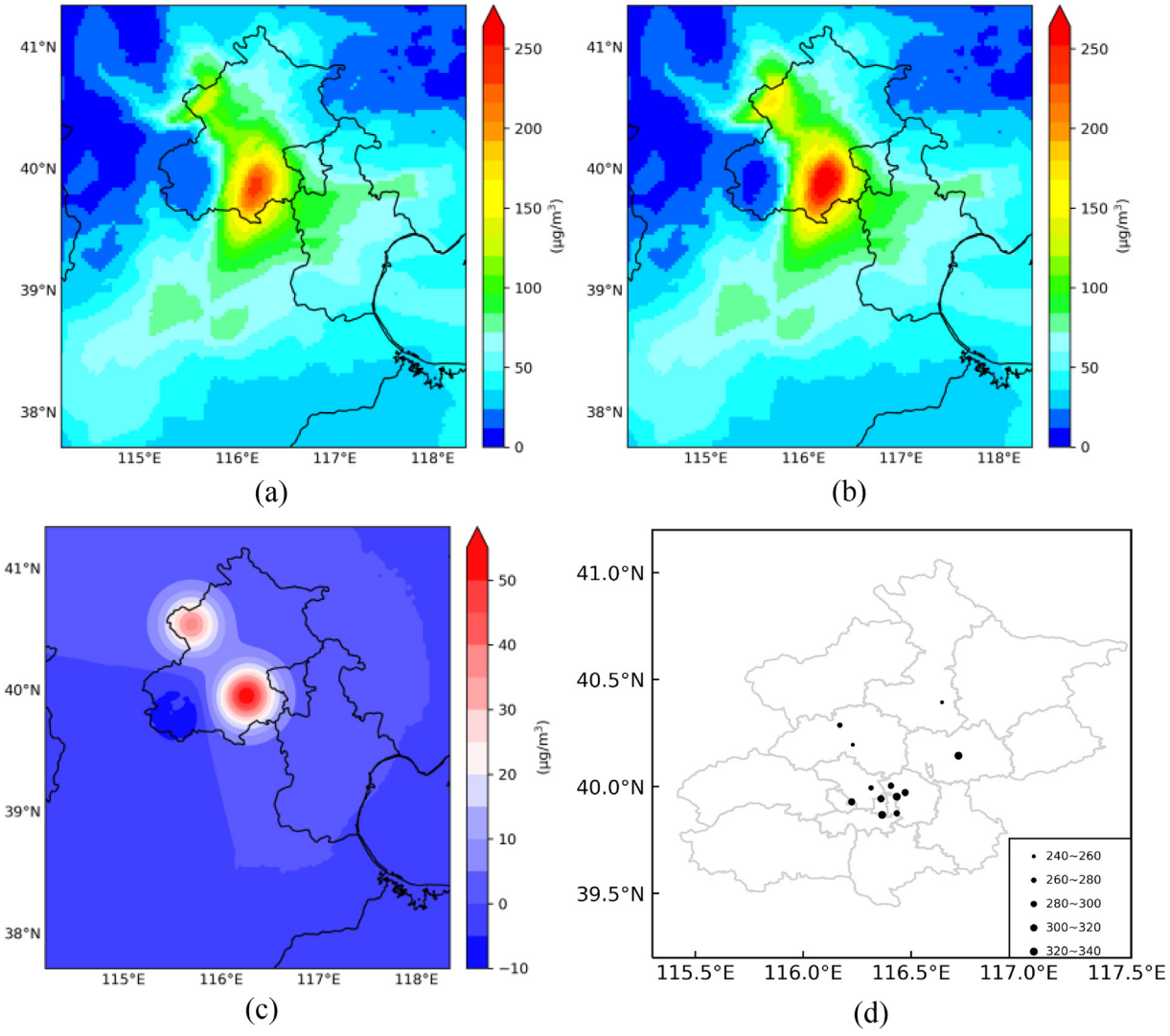

Fig. 7. Distribution of six hourly averaged simulated $PM_{2.5}$ concentrations from NoDA (a) and DA (b) experiments, increments (c) and surface observations (d) during 12:00–18:00 UTC on March 13, 2018.

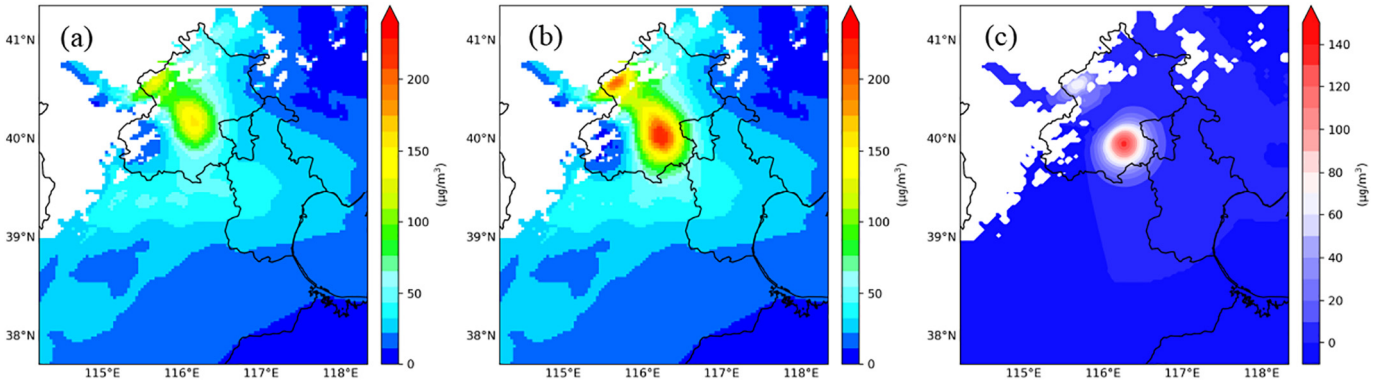

Fig. 8. As in Figure 7, except for 925 hPa and no observation.

Fig. 9). Larger positive increments of the five species are located in northwest and south central Beijing, which are similar to those of $PM_{2.5}$ presented above. In addition, the increments vary substantially across the species and span several orders of magnitude. Specifically, incremental magnitudes of NO_3^- and OIN are approximately ten times those of other species. Of the five species, increments of NO_3^- and OIN are the largest, and those of SO_4^{2-} and EC are the smallest; this corresponds with the differences in species ratios to $PM_{2.5}$ in Beijing. The latest observation results from Tan et al. (2018) revealed that the driving specie of pollution during the fall and winter of 2014 in Beijing is respectively nitrate, which is the largest contributor to incremental $PM_{2.5}$. The results of lidar DA analysis in this paper during the heavy haze episode in Beijing are consistent with those of Tan et al. (2018).

Improvements in the 3D structure of $PM_{2.5}$ are very important for analyzing the formation mechanism of haze and forecasting the air quality in the BTH region. We thus investigated the vertical profiles of average $PM_{2.5}$ concentrations and their increments from the NoDA and DA experiments during 12:00–18:00 UTC on March 13, 2018 (Fig. 10). Compared to the NoDA experiment, lidar DA provided evident improvements from the surface to the height of 1200 m in the planetary boundary layer over Beijing and the surrounding area. The largest increment of ~150 $\mu g \cdot m^{-3}$ occurred at 600 m with a horizontal scope of ~50 km, which corresponds to the horizontal length scale. Therefore, lidar DA is shown to evidently improve the vertical distribution of $PM_{2.5}$ and its species in the initial field of the CTMs, compared to the other DA.

4.2. Evaluation of forecasts

To further evaluate the lidar DA impact on aerosol forecasting, we compared 25 h forecasts of domain-averaged $PM_{2.5}$ concentrations from NoDA and DA experiments to observations obtained at 12 stations

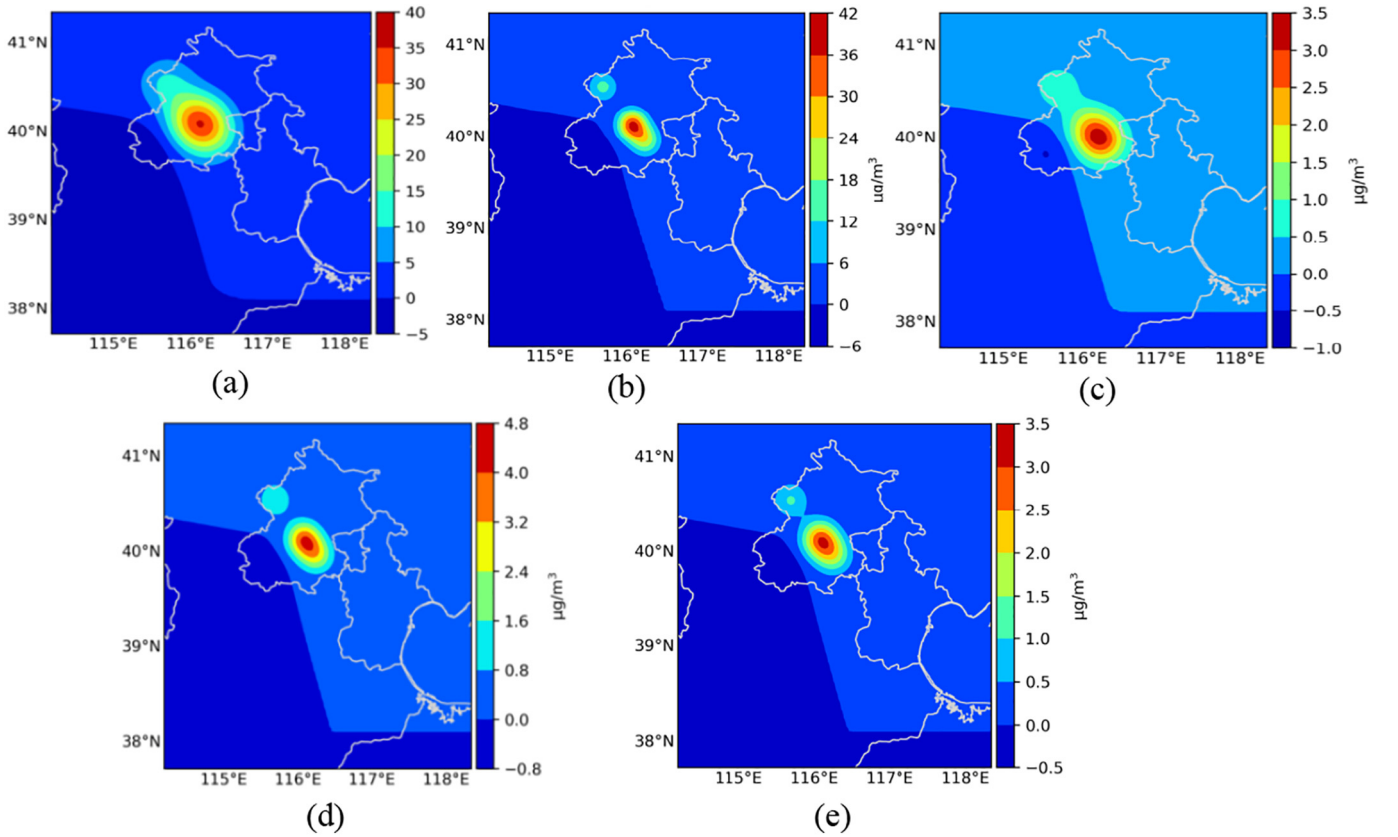

Fig. 9. Distribution of six hourly averaged $PM_{2.5}$ increments in: NO_3^- (a), OIN (b), SO_4^{2-} (c), OC (d), EC (e) during 12:00–18:00 UTC on March 13, 2018.

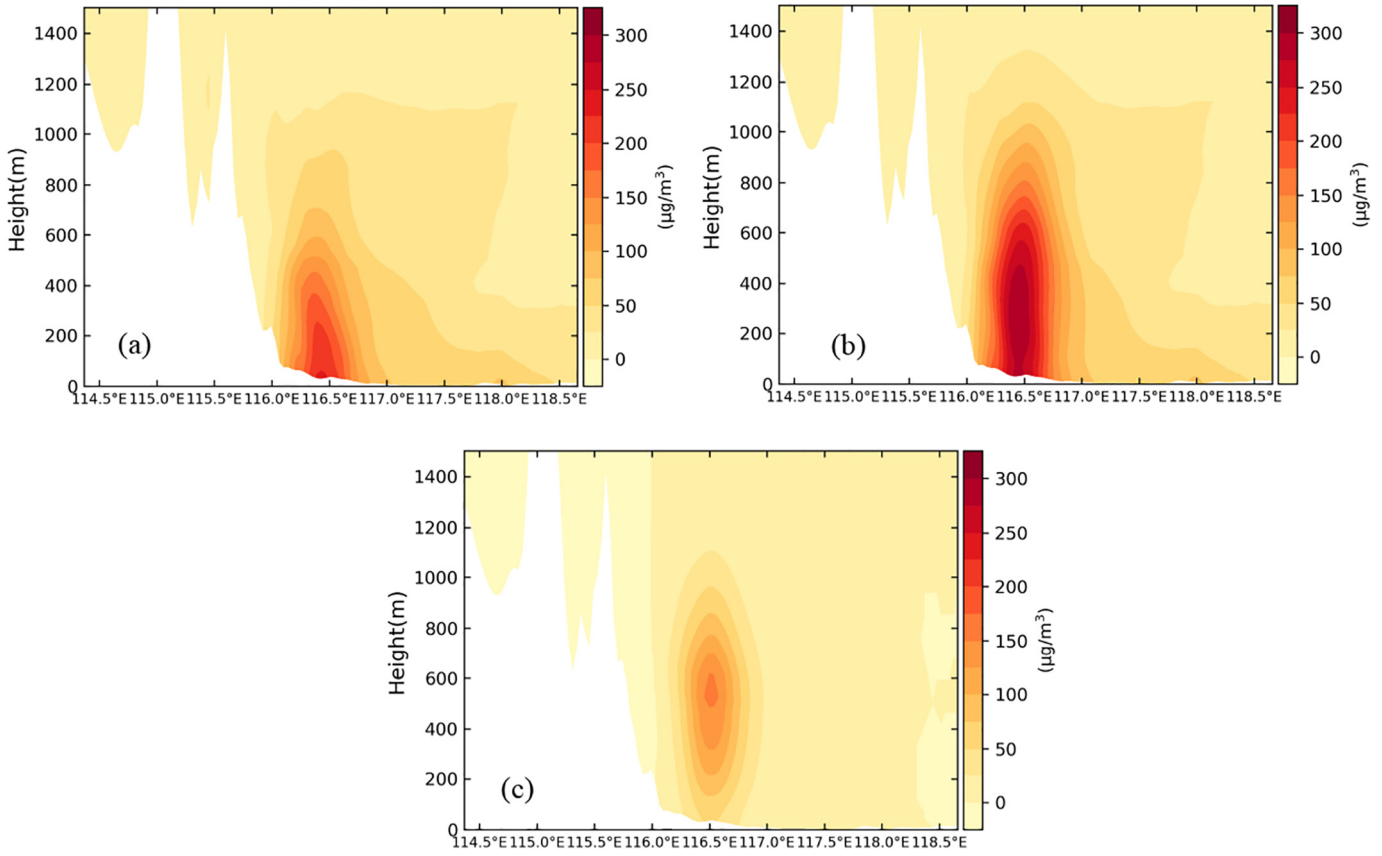

Fig. 10. Meridional vertical cross section at 39.73°N for six hourly averaged simulated $PM_{2.5}$ concentrations from NoDA (a) and DA (b) experiments, and the increment (c) during 12:00–18:00 UTC on March 13, 2018. Blank area denotes terrain.

from 12:00 UTC on March 13 to 13:00 UTC on March 14, 2018, and computed the RMSE of forecasts (Fig. 11). After lidar DA valid at 12:00 UTC on March 13, 6–12 h $PM_{2.5}$ forecasts are close to observations, while those without DA are far lower than observations during the same period (Fig. 11a). However, after 12 h, the two sets of forecasts (from the NoDA and DA experiments) become closer and are lower than those of observations. Compared to surface observations, the RMSEs of $PM_{2.5}$ forecasts with and without lidar DA decrease with the forecast duration up to 15 h, but then reduce rapidly at 1–12 h (Fig. 11b). RMSE for 1–15 h with lidar DA are all lower than that of the NoDA experiment. The above results suggest that the effective time period for using lidar DA in $PM_{2.5}$ forecasts is 15 h, and results are similar to those using aircraft data assimilation (Zang et al., 2016).

Fig. 12 shows scatter plots of 6–25 h $PM_{2.5}$ forecasts from NoDA and DA experiments after the last assimilation time versus surface observations at 12 stations in Beijing. It is evident that most of the forecast $PM_{2.5}$ concentrations from the NoDA experiment are less than observations, particularly when measurements are >200 $\mu g \cdot m^{-3}$. To be specific, forecasts made without lidar DA are remarkably underestimated, especially during the heavy haze period. Although with lidar DA, the $PM_{2.5}$ forecasts are closer to observations, and the underestimations at high concentrations (>300 $\mu g \cdot m^{-3}$) are remarkably improved, the forecasts

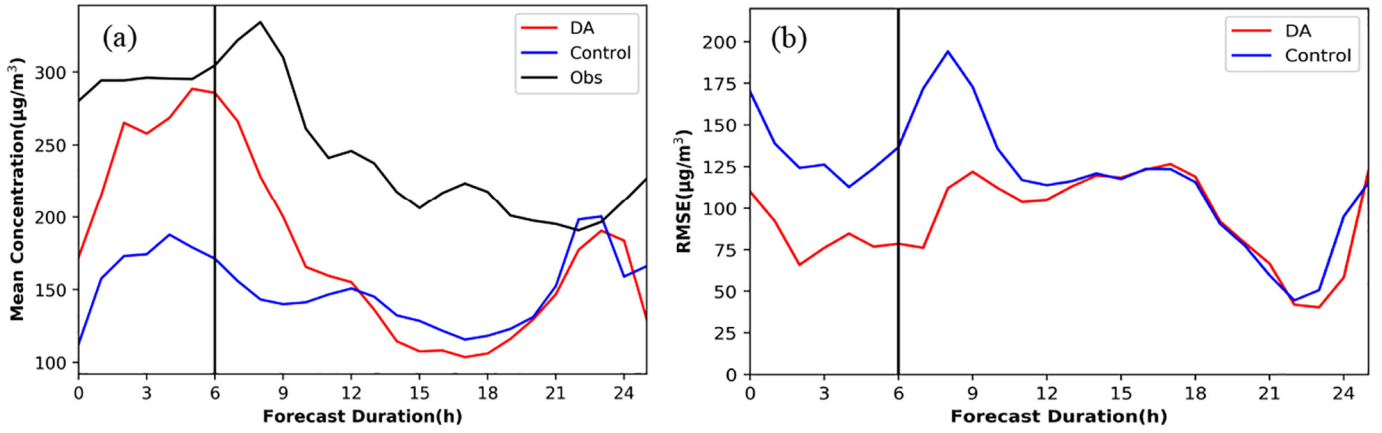

Fig. 11. Time series of domain-averaged forecast $PM_{2.5}$ concentrations (a) from the NoDA and DA experiment and observations, and their corresponding RMSE (b) at 12 stations in Beijing. Black line at 6th hour indicates final assimilation time.

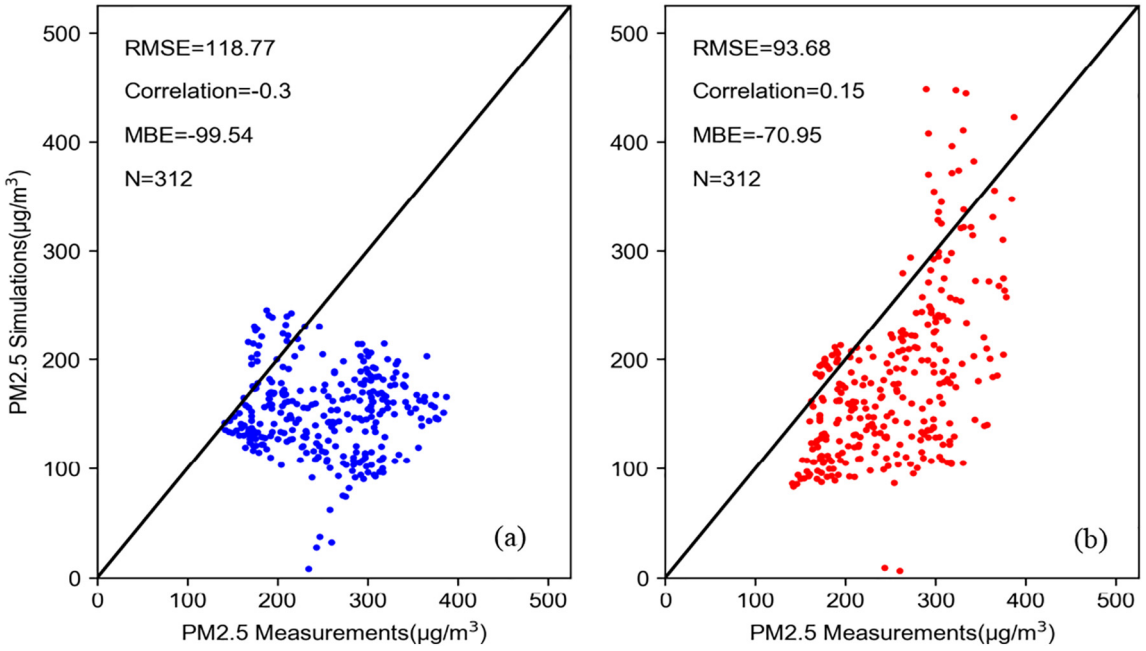

Fig. 12. Scatter plot between 6 and 25 h $PM_{2.5}$ forecasts from NoDA (a) and DA (b) experiments and observations at 12 stations in Beijing.

are also underestimated when observations fall between 100 $\mu g \cdot m^{-3}$ and 300 $\mu g \cdot m^{-3}$; however, it is considered that this could be caused by the uncertainty in the emissions inventory. There is a negative correlation coefficient between $PM_{2.5}$ forecasts without DA and observations, but there are evident improvements with lidar DA and correlation coefficient is positive and has a significant reliability level.

We then analyzed the probability distribution function (PDF) of the 6–25 h $PM_{2.5}$ forecast bias from the NoDA and DA experiments after the final assimilation time at 12 stations in Beijing (Fig. 13). The $PM_{2.5}$ forecasts bias from the NoDA experiment have a wide probability scope with ranges of $-250\,\mu g \cdot m^{-3}$ to $-20\,\mu g \cdot m^{-3}$, while most of the forecast biases after lidar DA fall between $-80\,\mu g \cdot m^{-3}$ and $-20\,\mu g \cdot m^{-3}$ and the probability is obviously higher than that without DA. This shows that there is an obvious decrease in the surface $PM_{2.5}$ forecast bias from the lidar DA experiment, and the underestimation in the NoDA experiment is remarkably improved. We also computed other statistical indicators (Table. 3) following the formulations presented in Wang et al. (2014b): the RMSE, mean fractional bias (MFB), mean fractional error (MFE), mean bias error (MBE) and correlation coefficients (CORR). The difference between 6 and 25 h averaged $PM_{2.5}$ forecasts at 12 stations with and without lidar DA and the mean observations

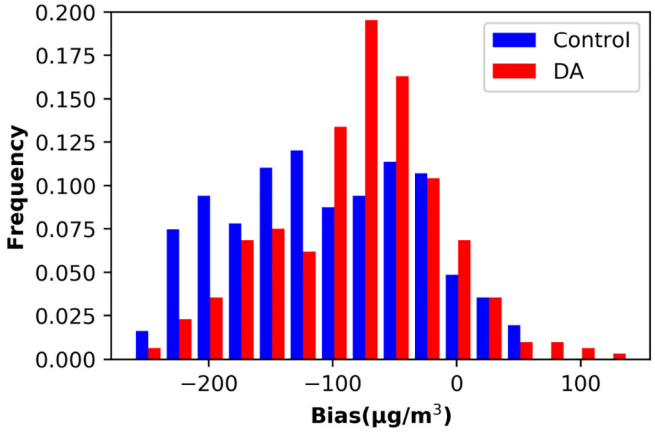

Fig. 13. PDF of 6–25 h $PM_{2.5}$ forecast bias from NoDA and DA experiments at 12 stations in Beijing.

are respectively $-58.48\,\mu g \cdot m^{-3}$ and $-87.42\,\mu g \cdot m^{-3}$. With lidar DA, the RMSE, MBE, MFB, and MFE is respectively reduced by 25.09 $\mu g \cdot m^{-3}$, 28.59 $\mu g \cdot m^{-3}$, 12% and 11%, while the CORR is increased by 0.45. These results suggest that the averaged $PM_{2.5}$ forecasting concentration with lidar DA is closer to the observations than with NoDA, and the temporal variation tendency of the $PM_{2.5}$ forecast is more consistent with observations.

5. Summary and discussion

A lidar observation experiment was conducted in Beijing during the pollution episode that occurred on March 13–15, 2018, and extinction coefficient data were acquired from four lidar stations. The vertical profiles of extinction coefficients were assimilated based on the 3DVAR system and CRTM model. Surface $PM_{2.5}$ observational data obtained at 12 stations in Beijing were then used to illustrate the impact of the lidar extinction coefficient DA on the analysis and subsequent forecast of the 3D aerosol structure.

Following the method presented in Li et al. (2013) and Zang et al. (2016), we constructed control variables based on eight aerosol species in four size bins within the MOSAIC scheme and established the BECs of all eight species for the 3DVAR system. To compute the observation operator between the aerosol species concentrations of model layers and the vertical profiles of the extinction coefficient observed using lidar, the CRTM and its tangent-linear, adjoint model were employed. A vertical-layer CRTM-AOD observation operator based on the vertical profiles of the extinction coefficient from lidar was developed to calculate the extinction coefficient using aerosol profiles simulated by the WRF-Chem model and the Jacobian of the extinction coefficient with respect to aerosol mass concentrations in every model layer. The improved efficiency of the newly developed lidar DA system was then demonstrated by applying it to a pollution episode that occurred in Beijing in March 2018, and assimilated analyses and subsequent forecasts were validated against surface $PM_{2.5}$ observation data from CNEMC. The lidar DA experiment that began at 12:00 UTC on March 13 assimilated the vertical profiles of the extinction coefficient from four in situ lidar stations in Beijing. The analysis field was then used to initialize WRF-Chem forecasts. As a reference, a control experiment without DA (NoDA) was also conducted from 00:00 UTC on March 13 to 00:00 UTC on March 15, 2018 with a 12 h spin-up time.

Table 3
Statistical indicators of 6–25 h $PM_{2.5}$ forecast concentrations from NoDA and DA experiments compared to observations at 12 stations in Beijing (sample number is 312).

Experiment	Mean observation $\mu g \cdot m^{-3}$	Mean simulation $\mu g \cdot m^{-3}$	RMSE $\mu g \cdot m^{-3}$	CORR	MFB %	MFE %	MBE $\mu g \cdot m^{-3}$
Control	238.42	151.0	118.77	−0.3	−49	51	−99.54
DA		179.94	93.68	0.15	−37	40	−70.95

The comparison with hourly surface $PM_{2.5}$ observations showed that forecasts without lidar DA were remarkably underestimated, especially during the heavy haze period. However, $PM_{2.5}$ forecasts with lidar DA were closer to observations and the model low bias was remarkably reduced, especially when the observations were larger than 300 $\mu g \cdot m^{-3}$. Significantly, the vertical distribution of $PM_{2.5}$ concentrations in Beijing showed obvious improvement from the surface to a height of 1200 m, and improvements in NO_3^- were the most significant of the five aerosol species; these results are consistent with other observations recorded during the same heavy haze episode in Beijing. In addition, the forecast skill improvement persisted for 15 h. These results suggest that the use of lidar DA would be effective in improving regional air quality forecasts and gaining a deeper understanding of the 3D structure of aerosols during heavy haze periods, if more ground-based lidar observation data could be obtained over the BTH region. Because four lidars are concentrated in the urban area of Beijing where emission intensity is very high, impacts of emission may be cover up the improvements of lidar DA in a certain degree and result in the limited effective time period for using lidar DA. We will assimilate more available lidar data and investigate the improvement effects of lidar DA in the clean areas where emission impacts are smaller in the future.

Further investigations are needed to improve the assimilation of NO_3^-, NH_4^+ and SO_4^{2-} in the observation operator, because the optical properties of these three species may differ to some degree. We therefore intend to employ a superior aerosol optical properties model, such as the MOPSMAP (Gasteiger and Wiegner, 2018), to advance the assimilation efficiency of the above three species in lidar DA. In addition, data quality control is very important for DA; therefore, direct assimilation of raw liar signals may be more effective at reducing errors derived from signals to extinction coefficients (Wang et al., 2014a, 2014b). In future work, we intend to develop an assimilation method for the raw lidar signal based on the 3DVAR system presented in this paper.

Acknowledgments

This work was jointly supported by the National Key Research and Development Program of China (2017YFC1501702), the National Natural Science Foundation of China (91644223), the National Research Program for Key Issues in Air Pollution Control (DQGG0104), the Scientific and Technological Development Funds from Chinese Academy of Meteorological Sciences (2018KJ042), and the Fundamental Research Funds from the Chinese Academy of Meteorological Sciences (2016Y005). The authors acknowledge Tsinghua University for providing the emissions inventory and China National Environmental Monitoring Centre for providing surface $PM_{2.5}$ observation data. The authors would also like to thank the anonymous reviewers for their constructive suggestions and comments.

References

Adhikary, B., Kulkarni, S., D'allura, A., Tang, Y., Chai, T., Leung, L.R., Qian, Y., Chung, C.E., Ramanathan, V., Carmichael, G.R., 2008. A regional scale chemical transport modeling of Asian aerosols with data assimilation of AOD observations using optimal interpolation technique. Atmos. Environ. 42 (37), 8600–8615.

Benedetti, A., Morcrette, J.J., Boucher, O., Dethof, A., Engelen, R.J., Fisher, M., Flentje, H., Huneeus, N., Jones, L., Kaiser, J.W., Kinne, S., Mangold, A., Razinger, M., Simmons, A.J., Suttie, M., 2009. Aerosol analysis and forecast in the European Centre for Medium-Range Weather Forecasts Integrated Forecast System: 2. Data assimilation. J. Geophys. Res. 114, D13205.

Böckmann, C., Wandinger, U., Ansmann, A., Bösenberg, J., Amiridis, V., Boselli, A., Delaval, A., De Tomasi, F., Frioud, M., Grigorov, I.V., Hågård, A., Horvat, M., Iarlori, M., Komguem, L., Kreipl, S., Larchevêque, G., Matthias, V., Papayannis, A., Pappalardo, G., Rocadenbosch, F., Rodrigues, J.A., Schneider, J., Shcherbakov, V., Wiegner, M., 2004. Aerosol lidar intercomparison in the framework of the EARLINET project. 2. Aerosol backscatter algorithms. Appl. Opt. 43 (4), 977–989.

Chen, F., Dudhia, J., 2001. Coupling an advanced land surface hydrology model with the Penn State/NCAR MM5 modeling system. Part I: model description and implementation. Mon. Weather Rev. 129 (4), 569–585.

China National Environmental Monitoring Centre, 2012. The National Urban Air Quality Real-time Publishing Platform. http://113.108.142.147:20035/emcpublish.

Collins, W.D., Rasch, P.J., Eaton, B.E., Khattatov, B.V., Lamarque, J.-F., 2001. Simulating aerosols using a chemical transport model with assimilation of satellite aerosol retrievals: methodology for INDOEX. J. Geophys. Res. 106, 7313–7336.

Denby, B., Schaap, M., Segers, A., Builtjes, P., Horalek, J., 2008. Comparison of two data assimilation methods for assessing PM_{10} exceedances on the European scale. Atmos. Environ. 42, 7122–7134.

Emmons, L.K., Walters, S., Hess, P.G., Lamarque, J.F., Pfister, G.G., Fillmore, D., Granier, C., Guenther, A., Kinnison, D., Laepple, T., Orlando, J., Tie, X., Tyndall, G., Wiedinmyer, C., Baughcum, S.L., Kloster, S., 2010. Description and evaluation of the model for ozone and related chemical tracers, version 4 (mozart-4). Geosci. Model Dev. 3, 43–67.

Fast, J.D., Gustafson Jr., W.I., Easter, R.C., Zaveri, R.A., Barnard, J.C., Chapman, E.G., Grell, G.A., Peckham, S.E., 2006. Evolution of ozone, particulates, and aerosol direct radiative forcing in the vicinity of Houston using a fully coupled meteorology-chemistry-aerosol model. J. Geophys. Res. 111, D21305.

Gasteiger, J., Wiegner, M., 2018. MOPSMAP v1.0: a versatile tool for the modeling of aerosol optical properties. Geosci. Model Dev. 11, 2739–2762.

Generoso, S., Bréon, F.-M., Chevallier, F., Balkanski, Y., Schulz, M., Bey, I., 2007. Assimilation of POLDER aerosol optical thickness into the LMDz-INCA model: implications for the Arctic aerosol burden. J. Geophys. Res. 112, D02311.

Grell, G.A., Freitas, S.R., 2014. A scale and aerosol aware stochastic convective parameterization for weather and air quality modeling. Atmos. Chem. Phys. 14, 5233–5250.

Grell, G.A., Peckham, S.E., Schmitz, R., McKeen, S.A., Frost, G., Skamarock, W.C., Eder, B., 2005. Fully coupled "online" chemistry within the WRF model. Atmos. Environ. 39, 6957–6975.

Han, Y., van Delst, P., Liu, Q., Weng, F., Yan, B., Treadon, R., Derber, J., 2006. JCSDA Community Radiative Transfer Model (CRTM)—Version 1, NOAA Tech. Rep. NESDIS 122. 33 pp. NOAA, Silver Spring, Md.

Hong, S.Y., Lim, J.-O., 2006. The WRF Single-Moment 6-Class Microphysics Scheme (WSM6). J. Kor. Meteorol. Soc. 42, 129–151.

Iacono, M.J., Delamere, J.S., Mlawer, E.J., Shephard, M.W., Clough, S.A., Collins, W.D., 2008. Radiative forcing by long-lived greenhouse gases: calculations with the AER radiative transfer models. J. Geophys. Res. 113, D13103.

Jiménez, P.A., Dudhia, J., González-Rouco, J.F., Navarro, J., Montávez, J.P., Garcia-Bustamante, E., 2012. A revised scheme for the WRF surface layer formulation. Mon. Weather Rev. 140 (3), 898–918.

Li, Z., Zang, Z., Li, Q.B., Chao, Y., Chen, D., Ye, Z., Liu, Y., Liou, K.N., 2013. A three-dimensional variational data assimilation system for multiple aerosol species with WRF/Chem and an application to $PM_{2.5}$ prediction. Atmos. Chem. Phys. 13, 4265–4278.

Lin, C., Wang, Z., Zhu, J., 2008. An Ensemble Kalman Filter for severe dust storm data assimilation over China. Atmos. Chem. Phys. 8, 2975–2983.

Liu, Q., Weng, F., 2006. Advanced doubling-adding method for radiative transfer in planetary atmosphere. J. Atmos. Sci. 63 (12), 3459–3465.

Liu, Z., Liu, Q., Lin, H.-C., Schwartz, C.S., Lee, Y.-H., Wang, T., 2011. Three-dimensional variational assimilation of MODIS aerosol optical depth: implementation and application to a dust storm over East Asia. J. Geophys. Res. 116, D23206.

Lorenc, A.C., 1981. A global three-dimensional multivariate statistical interpolation scheme. Mon. Weather Rev. 109 (4), 701–721.

Mangold, A., De Backer, H., De Paepe, B., Dewitte, S., Chiapello, I., Derimian, Y., Kacenelenbogen, M., Léon, J.-F., Huneeus, N., Schulz, M., Ceburnis, D., O'Dowd, C., Flentje, H., Kinne, S., Benedetti, A., Morcrette, J.-J., Boucher, O., 2011. Aerosol analysis and forecast in the European Centre for Medium-Range Weather Forecasts Integrated Forecast System: 3. Evaluation by means of case studies. J. Geophys. Res. 116, D03302.

Morcrette, J.J., Boucher, O., Jones, L., Salmond, D., Bechtold, P., Beljaars, A., Benedetti, A., Bonet, A., Kaiser, J.W., Razinger, M., Schulz, M., Serrar, S., Simmons, A.J., Sofiev, M., Suttie, M., Tompkins, A.M., Untch, A., 2009. Aerosol analysis and forecast in the European Centre for Medium-Range Weather Forecasts Integrated Forecast System: Forward modeling. J. Geophys. Res. 114 D06206.

Niu, T., Gong, S.L., Zhu, G.F., Liu, H.L., Hu, X.Q., Zhou, C.H., Wang, Y.Q., 2008. Data assimilation of dust aerosol observations for the CUACE/dust forecasting system. Atmos. Chem. Phys. 8, 3473–3482.

Pagowski, M., Grell, G.A., 2012. Experiments with the assimilation of fine aerosols using an ensemble Kalman filter. J. Geophys. Res. 117, 1–15.
Pagowski, M., Grell, G.A., McKeen, S.A., Peckham, S.E., Devenyi, D., 2010. Three-dimensional variational data assimilation of ozone and fine particulate matter observations: some results using the weather research and forecasting-chemistry model and grid-point statistical interpolation. Q. J. R. Meteorol. Soc. 136, 2013–2024.
Parrish, D.F., Derber, J.C., 1992. The National Meteorological Center's spectral statistical-interpolation analysis scheme. Mon. Weather Rev. 120, 1747–1763.
Schutgens, N.A.J., Miyoshi, T., Takemuraa, T., Nakajima, T., 2010. Applying an ensemble Kalman filter to the assimilation of AERONET observations in a global aerosol transport model. Atmos. Chem. Phys. 10, 2561–2576.
Sekiyama, T.T., Tanaka, T.Y., Shimizu, A., Miyoshi, T., 2010. Data assimilation of CALIPSO aerosol observations. Atmos. Chem. Phys. 10, 39–49.
Sugimoto, N., Uno, I., 2009. Observation of Asian dust and airpollution aerosols using a network of ground-based lidars (ADNet): realtime data processing for validation/assimilation of chemical transport models. IOP C. Ser. Earth Environ. 7, 012003.
Tan, T., Hu, M., Li, M., Guo, Q., Wu, Y., Fang, X., Gu, F., Wang, Y., Wu, Z., 2018. New insight into $PM_{2.5}$ pollution patterns in Beijing based on one-year measurement of chemical compositions. Sci. Total Environ. 621, 734–743.
Tombette, M., Mallet, V., Sportisse, B., 2009. PM_{10} data assimilation over Europe with the optimal interpolation method. Atmos. Chem. Phys. 9, 57–70.
Wang, Y., Sartelet, K.N., Bocquet, M., Chazette, P., 2013. Assimilation of ground versus lidar observations for PM_{10} forecasting. Atmos. Chem. Phys. 13, 269–283.
Wang, Y., Sartelet, K.N., Bocquet, M., Chazette, P., 2014a. Modelling and assimilation of lidar signals over Greater Paris during the MEGAPOLI summer campaign. Atmos. Chem. Phys. 14, 3511–3532.
Wang, Y., Sartelet, K.N., Bocquet, M., Chazette, P., Sicard, M., Amico, G.D., Léon, J.F., Alados-Arboledas, L., Amodeo, A., Augustin, P., Bach, J., Belegante, L., Binietoglou, I., Bush, X., Comerón, A., Delbarre, H., García-Vízcaino, D., Guerrero-Rascado, J.L., Hervo, M., Iarlori, M., Kokkalis, P., Lange, D., Molero, F., Montoux, N., Muñoz, A., Muñoz, C., Nicolae, D., Papayannis, A., Pappalardo, G., Preissler, J., Rizi, V., Rocadenbosch, F., Sellegri, K., Wagner, F., Dulac, F., 2014b. Assimilation of lidar signals: application to aerosol forecasting in the western Mediterranean basin. Atmos. Chem. Phys. 14, 12031–12053.
Xiang, Y., 2018. Study on the Three-dimensional Assimilation and Comprehensive Analysis of the Regional Network Data of Lidar, A dissertation for doctor's degree in the University of Science and Technology of China.
You, W., 2017. $PM_{2.5}/PM_{10}$ Retrieval and Assimilation Based on Satellite AOD. A dissertation for doctor's degree in the. National University of Defense Technology.
Yu, H., Dickinson, R.E., Chin, M., Kaufman, Y.J., Geogdzhayev, B., Mishchenko, M.I., 2003. Annual cycle of global distributions of aerosol optical depth from integration of MODIS retrievals and GOCART model simulations. J. Geophys. Res. 108, 4128.
Yumimoto, K., Uno, I., Sugimoto, N., Shimizu, A., Satake, S., 2007. Adjoint inverse modeling of dust emission and transport over East Asia. Geophys. Res. Lett. 34.
Yumimoto, K., Uno, I., Sugimoto, N., Shimizu, A., Liu, Z., Winker, D.M., 2008. Adjoint inversion modeling of Asian dust emission using lidar observations. Atmos. Chem. Phys. 8 (11), 2869–2884.
Zang, Z.L., Li, Z.J., Pan, X.B., Hao, Z.L., You, W., 2016. Aerosol data assimilation and forecasting experiments using aircraft and surface observations during CalNex. Tellus Ser. B Chem. Phys. Meteorol. 68, 29812.
Zhang, J., Reid, J.S., Westphal, D., Baker, N., Hyer, E., 2008. A system for operational aerosol optical depth data assimilation over global oceans. J. Geophys. Res. 113, D10208.
Zhang, Q., Streets, D.G., Carmichael, G.R., He, K.B., Huo, H., Kannari, A., Klimont, Z., Park, I.S., Reddy, S., Fu, J.S., Chen, D., Duan, L., Lei, Y., Wang, L.T., Yao, Z.L., 2009. Asian emissions in 2006 for the NASA INTEX-B mission. Atmos. Chem. Phys. 9, 5131–5153.
Zhang, J., Campbell, J.R., Reid, J.S., Westphal, D.L., Baker, N.L., Campbell, W.F., Hyer, E.J., 2011. Evaluating the impact of assimilating CALIOP-derived aerosol extinction profiles on a global mass transport model. Geophys. Res. Lett. 38, L14801.
Zhao, H.Y., Zhang, Q., Guan, D.B., Davis, S.J., Liu, Z., Huo, H., Lin, J.T., Liu, W.D., He, K.B., 2015. Assessment of China's virtual air pollution transport embodied in trade by using a consumption-based emission inventory. Atmos. Chem. Phys. 15 (10), 5443–5456.
Zheng, H.T., 2018. Improvement of $PM_{2.5}$ Forecast by Data Assimilation of Ground and Lidar Observation. A dissertation for doctor's degree in the. University of Science and Technology of China.